3D osteocyte lacunar morphometry of human bone biopsies with high resolution microCT: from monoclonal gammopathy to newly diagnosed multiple myeloma

Inés Moreno-Jiménez[1*], Sharen Heinig[1], Unai Heras[2,3], Daniela Simone Maichl[4], Susanne Strifler[4], Ellen Leich[5,6], Stéphane Blouin[7], Peter Fratzl[1], Nadja Fratzl-Zelman[7], Franziska Jundt[4,6*#], Amaia Cipitria[1,2,8*#]

[1] Max Planck Institute of Colloids and Interfaces, Department of Biomaterials, 14476 Potsdam, Germany

[2] Group of Bioengineering in Regeneration and Cancer, Biogipuzkoa Health Research Institute, 20014 San Sebastian, Spain.

[3] Department of Cell Biology and Histology, Faculty of Medicine and Nursing, University of the Basque Country UPV/EHU, 48940 Leioa, Spain

[4] Department of Internal Medicine II, University Hospital Würzburg, 97080 Würzburg, Germany

[5] Institute of Pathology, University of Würzburg, 97080 Würzburg, Germany

[6] Comprehensive Cancer Center Mainfranken, 97080 Würzburg, Germany

[7] Ludwig Boltzmann Institute of Osteology at the Hanusch Hospital of OEGK and AUVA Trauma Centre Meidling, Vienna, Austria.

[8] IKERBASQUE, Basque Foundation for Science, 48009 Bilbao, Spain.

(*) Correspondence to: inesmorenojimenez@gmail.com; jundt_f@ukw.de; amaia.cipitria@mpikg.mpg.de; amaia.cipitriasagardia@bio-gipuzkoa.eus

(#) These authors contributed equally to this work

Abstract

Osteocytes are mechanosensitive, bone-embedded cells which are connected via dendrites in a lacuno-canalicular network and regulate bone resorption and formation balance. Alterations in osteocyte lacunar volume, shape and density have been identified in conditions of aging, osteoporosis and osteolytic bone metastasis, indicating patterns of impaired bone remodeling, osteolysis and disease progression. Osteolytic bone disease is a hallmark of the hematologic malignancy multiple myeloma (MM), in which monoclonal plasma cells in the bone marrow disrupt the bone homeostasis and induce excessive resorption at local and distant sites. Qualitative and quantitative changes in the 3D osteocyte lacunar morphometry have not yet been evaluated in MM, nor in the precursor conditions monoclonal gammopathy of undetermined significance (MGUS) and smoldering multiple myeloma (SMM). In this study, we characterized the osteocyte lacunar morphology in trabecular bone of the iliac crest at the ultrastructural level using high resolution microCT in human bone biopsy samples of three MGUS, two SMM and six newly diagnosed MM. In MGUS, SMM and MM we found a trend for lower lacunar density and a shift towards larger lacunae with disease progression (higher 50% cutoff of the lacunar volume cumulative distribution) in the small osteocyte lacunae 20-900 μm^3 range compared to control samples. In the larger lacunae 900-3000 μm^3 range, we detected significantly higher lacunar density and microporosity in the MM group compared to the MGUS/SMM group. Regarding the shape distribution, the MGUS/SMM group showed a trend for flatter, more elongated and anisotropic osteocyte lacunae compared to the control group. Altogether, our findings suggest that osteocytes in human MM bone disease undergo changes in their lacunae density, volume and shape, which could be an indicator for osteolysis and disease progression. Future studies are needed to understand whether alterations of the lacunae architecture affect the mechanoresponsiveness of osteocytes and ultimately bone adaptation and fracture resistance in MM and its precursors conditions.

Keywords

Osteocyte lacuna; Morphometry; High resolution microCT; Human bone biopsy; Multiple myeloma (MM); Monoclonal gammopathy of undetermined significance (MGUS); Smoldering multiple myeloma (SMM)

1. Introduction

Osteocytes are bone-embedded cells, connected via dendrites in a lacuno-canalicular network (LCN). They act as local sentinels in response to external stimuli and regulate the balance between bone resorption/formation [1]. In response to mechanical strain, osteocytes orchestrate the remodeling of the perilacunar bone matrix and thereby change shape and size of their lacunae [2]. Lacunar volume, shape and density were influenced by changes of the surrounding environment, either mechanically or chemically, and by aging or disease. Changes in lacuna volume were observed after exposing mice to non-gravity [3] or after treatment with glucocorticoid slowing down bone metabolism [4], resulting in both cases in larger lacunae. In contrast, smaller lacunar size and lacunar density were observed in rodent models of aging [5] and osteoporosis, where the effect of different anti-resorptive drugs in intracortical microporosities was evaluated [6]. In humans, a decline in lacunar density was observed with aging, while a significantly higher density was found in osteoporotic bone compared to controls [7]. A recent study with human bone biopsy samples of healthy individuals across the life span revealed decreasing osteocyte lacunae density and porosity with aging, before the peak bone mass at 30 years, which then stabilized or even increased after this age [8]. Furthermore, mineralized osteocyte lacunae (micropetrosis) were found increased with aging and osteoporosis, which was attributed to osteocyte apoptosis and improved with bisphosphonates treatment [9]. Changes in lacunar shape, notably becoming smaller and more spherical with age, were linked to aging, resulting in diminished local bone tissue strains, impacting bone mechanosensitivity and fracture resistance [2,10]. Noteworthy, abnormal morphological features were also detected in a large-scale assessment of adolescent idiopathic scoliosis, using high resolution microCT [11].

In cancer, osteocytes, as well as osteoblasts and osteoclasts, communicate with tumor cells and this generates a microenvironment that supports cancer cell growth and stimulates bone destruction [12]. Interactions between breast and prostate cancer cells and osteocytes influenced cancer cell migration and invasion potential and contributed to the establishment and progression of bone metastasis [13,14]. Also, breast cancer cells induced osteocyte apoptosis and altered osteocyte function [15]. Recently, a study of osteotropic cancers in rodents revealed that the spatial distribution of cortical bone microporosity, osteocyte lacunae volume and the LCN characteristics were influenced by the presence of tumor cells in osteolytic lesions [16]. Taken together, changes in the volume and shape of osteocyte lacunae are an indicator of osteolysis in bone metastasis of osteotropic cancers.

96 An example of an incurable malignancy of the bone marrow and bone is multiple myeloma
97 (MM), in which plasma cells producing monoclonal immunoglobulins disrupt the bone
98 homeostasis towards excessive bone resorption [17]. MM cells alter the bone marrow
99 environment by releasing signals that promote osteoclast activity, while inhibiting osteoblast
100 function [18,19]. There is evidence that MM cells also target osteocytes by enhancing apoptosis
101 and expression of sclerostin, an inhibitor of bone formation [20]. Even though MM cells
102 directly interact with osteocytes and vice versa, the consequences of these interactions on the
103 local bone microstructure are largely unknown [20].
104
105 In the clinical setting, two pre-symptomatic stages precede MM: (i) an initial phase named
106 monoclonal gammopathy of underdetermined significance' (MGUS), which can progress in
107 (ii) smoldering multiple myeloma (SMM). Both MGUS and SMM patients do not present
108 MM clinical symptoms (C.R.A.B. symptoms of MM: hypercalcemia, renal insufficiency,
109 anemia and/or osteolytic bone lesions[21]). In patients with MM, low-dose whole body
110 computed tomography (CT) scans are routinely used to detect osteolytic lesions and fractures
111 [22]. It remains, however, poorly understood whether bone microstructural changes precede the
112 osteolytic lesions.
113
114 To identify associations between changes in the bone microarchitecture and fractures, x-ray
115 absorptiometry measuring bone density or low-dose CT scans were used in two clinical
116 studies [23,24]. In one study, low-dose CT scans showed reduced radiodensity, trabecular
117 thickening and vertebral fractures, demonstrating that focal skeletal changes were
118 significantly associated with further skeletal damages [23]. Some earlier studies had attempted
119 to study bone trabecular thickness and separation in MM patients; however, the resolution
120 limit of clinical CT scans was an obstacle for this objective [25,26]. Our group used advanced
121 imaging techniques (high resolution microCT, synchrotron phase contrast-enhanced
122 microCT, confocal laser scanning microscopy) to evaluate the bone microstructure in an early
123 MM mouse model [27]. We showed irregular shaped osteocyte lacunae, altered osteocyte LCN
124 characteristics and local alterations of the extracellular matrix (ECM) with active erosion
125 sites [27]. Following on from this preclinical study, here we investigate human bone biopsies of
126 MGUS, SMM and newly diagnosed MM patients with high resolution microCT for
127 ultrastructural characterization of osteocyte lacunar morphology, to identify alterations that
128 can be linked to osteolysis and disease progression.
129

2. Materials and methods

2.1 Patient sample collection and clinical evaluation

The purpose of this study was to determine whether changes in osteocyte lacunae volume and shape distribution could be detected in mineralized bone biopsy samples from patients with MGUS, SMM and newly diagnosed MM. Patients with MGUS (n=3), SMM (n=2) and symptomatic MM (n=6) were diagnosed following the revised international staging system [22]. Clinical data from eleven patients including reports of the low-dose CT scans are given in Tables 1-3. Values in brackets show the normal range for the parameters. The investigators who performed the bench studies were blind to the patient information. This study was approved by the Ethics Committee of the University of Würzburg, Germany (76/13 and 82/20-am). Patients where included with an informed consent for the bone biopsy, with a known history of MGUS, SMM, symptomatic MM, lymphoma, leukemia, myelodysplastic syndrome, or myeloproliferative disorders. Patients receiving a bone biopsy based on other disease like a bone marrow carcinosis were excluded from the study. As control bone biopsy samples, two different data sets were used (Table 4). One Jamshidi bone biopsy sample (2 mm diameter) was obtained from a patient of the University Hospital Würzburg with myelodysplastic syndrome and no diagnosis of MGUS, SMM or MM. Three cylindrical transiliac samples (5 mm diameter) were obtained from an earlier study [8] on autopsy samples at the Ludwig Boltzmann-Institute of Osteology Vienna. Osteocyte lacunae characteristics were re-evaluated in the current study. For all control and disease bone biopsy samples, the trabecular bone compartment was analyzed and the cortical bone was excluded. Trabecular bone is the first contact region with MM cells and comprises the larger fraction of bone in Jamshidi biopsies. Cortical bone was not present in some biopsies, as we received left over tissue after diagnosis. Only biopsy samples containing sufficient amount of trabecular bone, which maintained sample integrity without loss of bone structure (bone debris) caused by the extraction procedure, were considered.

The patient clinical data (Tables 1-3) include: biopsy number, disease stage (MGUS, SMM or newly diagnosed MM), age, gender, immunoglobulin subtypes (heavy and light chains) secreted by malignant plasma cells, revised International Staging System (r-ISS), cytogenetic risk, M-protein secreted by plasma cells at time of diagnosis (g/L), heavy chain (mg/dL), involved serum free light chain (sFLC) (mg/L), ratio (involved/uninvolved sFLC), bone marrow infiltration (%) based on immunohistochemistry Syndecan-1 (CD138) with >60% corresponding to newly diagnosed MM, computed tomography findings of osteolytic lesions,

164 hemoglobin (g/dL), creatinine (mg/dL) and cytogenetic alterations by fluorescence in situ
165 hybridization (FISH), which allows for detection of genetic changes which are relevant for
166 the ISS stage. In addition, parameters describing the bone metabolism include: calcium
167 (mmol/L), alkaline phosphatase (U/L), phosphate (mmol/L) and finally, bone anti-resorption
168 treatment ongoing at the time of biopsy.
169
170 **2.2 Immunohistochemical detection of CD138 on decalcified bone paraffin sections**
171 Paraffin embedded human specimens were retrospectively collected from formalin-fixed
172 paraffin-embedded tissue of anonymized samples, archived at the Institute of Pathology,
173 University of Würzburg. Shortly, Jamshidi bone biopsy samples that were derived from the
174 clinical department of the University of Würzburg were fixed for 24 h in formalin,
175 decalcified for 24 h at 37°C using an EDTA-based approach, dehydrated with alcohol and
176 xylene and then embedded in paraffin.
177
178 For the immunohistochemical detection of CD138/Syndecan-1 expression, sections were
179 deparaffinized. The tissue was hybridized with an antibody against CD138/Syndecan-1
180 (clone MI15, mouse, #M7228, Agilent, Santa Clara, CA, USA), following standard
181 procedures by automated processing using the Tecan Evo Freedom stainer and the Dako
182 Advance system according to the manufacturer's protocol.
183
184 **2.3 Microcomputed tomography (microCT): image acquisition**
185 Specimens were scanned using an EasyTom micro/nano tomograph (RX solutions, France).
186 Low resolution scanning parameters were: 107 kV, 93 µA, 7 µm voxel size, frame rate of 3,
187 average frame of 5. High resolution scanning parameters were: 60 kV, 124 µA, 1-2 µm voxel
188 size, frame rate of 1, average frame of 5. Reconstruction of the 1120 projections/scan were
189 performed using RX Solutions X-Act software.
190
191 **2.4 Low resolution microCT: image analysis**
192 The overall bone biopsy morphology with particular focus on trabecular bone thickness was
193 analyzed with Dragonfly software, Version 2022.1 for [Windows]. Comet Technologies
194 Canada Inc., Montreal, Canada; software available at https://www.theobjects.com/dragonfly.
195 Low resolution microCT stack images (voxel size of 7 µm) were segmented using Otsu

196 thresholding (noise removal of these microCT images and objects was not necessary). A
197 mesh was then created from each individual region of interest (ROI) of the trabecular bone.
198 The trabecular bone strut thickness was automatically generated and measured from each
199 mesh by Dragonfly software. For this, we calculated the median, first and third quartile,
200 minimum and maximum values of about 3-5.5 10^6 local vertices created between boundary
201 points of each overall mesh. The software calculated these vertices as diameters of
202 hypothetical spheres that fit within each boundary points of the mesh. The trabecular bone
203 strut thickness distribution is depicted with a color code for each biopsy and as a box plot.
204
205 **2.5 High resolution microCT: image analysis**
206 The VOI within the high resolution scans were selected in such a way so that the bone
207 volume to be analyzed was maximized. The empty cavities within mineralized tissue
208 corresponding to osteocyte lacunae were segmented. Based on previous studies with healthy
209 trabecular bone [8,28–30], cavities smaller than 20 μm^3 and larger than 3000 μm^3 were
210 considered cracks or artifacts and excluded from the analysis.
211
212 2.5.1 Segmentation of osteocyte lacunae
213 The stack of high resolution microCT images (1-2 µm voxel size) was segmented using Otsu
214 thresholding in Dragonfly. For these images, noise removal was performed using 3D
215 smoothing (kernel of 3) as morphological operation. Next, the binary mask was used to
216 extract the pores. Osteocyte lacunae were filled in a copy of the binary mask using a filling
217 morphological operation. Next, the multi-ROI conversion tool of Dragonfly was used to
218 select each lacuna individually. This tool allowed to define each osteocyte lacuna as an
219 individual ROI, hence enabling the calculation of each lacunae volume and shape. The
220 generated binary images were then used for the quantitative analysis of lacunae volume and
221 shape with Python software (version 3.5). The script used was written in a Jupyter notebook
222 with Python software (version 3.7). External libraries not contained in the Anaconda
223 environment were installed from their repository. Micropores smaller than 20 μm^3 and larger
224 than 3000 μm^3 were considered cracks or artifacts and excluded from the analysis. For the
225 purpose of this study, two separate lacunar volume ranges were investigated: small lacunae
226 20-900 μm^3 (osteocyte lacunar microporosity characteristic of healthy bone [28,31]), and larger
227 lacunae 900-3000 μm^3 (microporosity potentially associated to bone disease).
228

229 2.5.2 Osteocyte lacunar volume analysis

230 For the osteocyte lacunar volume analysis, each segmented lacunar volume was calculated as
231 the total number of voxels times the volume of a single voxel. Based on this, we could define
232 the number of lacunae (Lc.N) of a given lacunar volume (Lc.V). We could also define the
233 total number of osteocyte lacunae (Lc.TN), total lacunar volume (Lc.TV) and trabecular bone
234 total volume (Tb.TV). This nomenclature and units are summarized in Table 5.

235

236 2.5.3 Normalized lacunar volume frequency distribution and lacunar density

237 To plot the lacunar volume frequency distribution, all lacunae within one sample were
238 stratified according to lacunar volume intervals. For a discrete lacunar volume interval of
239 20 μm^3, we quantified the number of osteocyte lacunae (Lc.N.) for that given size. For a
240 given lacunar volume (Lc.V), we quantified the lacunar number (Lc.N), normalized to the
241 trabecular bone total volume (Tb.TV) and excluding the total lacunar volume (Tb.TV-
242 Lc.TV), to account for size differences between samples, since larger samples have more
243 lacunae than smaller ones, as well as for potential differences in the trabecular bone
244 microporosity. The data is presented as the frequency in a histogram with a bin size of
245 20 μm^3. Furthermore, the lacunar density was calculated as the total number of osteocyte
246 lacunae (Lc.TN) normalized to the trabecular bone total volume and excluding lacunar total
247 volume (Tb.TV-Lc.TV), in other words, the summation of the osteocyte lacunar volume
248 frequency distribution. This was done for both ranges separately, small lacunae 20-900 μm^3
249 and larger lacunae 900-3000 μm^3.

250

251 2.5.4 Lacunar volume cumulative distribution

252 The cumulative distribution is calculated by sorting all osteocyte lacunae by volume, from
253 smallest to largest, and increasing the count of the fraction 1/N at each point, with N = length
254 of array. The cumulative lacunae volume distribution was plotted with respect to the lacunae
255 volume (Lc.V), with the x axis showing a given lacunae volume and the y axis showing the
256 cumulative volume. The 50% cutoff illustrating the specific volume below which half of all
257 osteocyte lacunae are contained, was marked with a dashed line.

258

259 2.5.5 Osteocyte lacunar microporosity analysis

The microporosity was calculated as the lacunar total volume (Lc.TV) divided by trabecular bone total volume (Tb.TV) for each group. This was done for both ranges separately, small lacunae 20-900 μm^3 and larger lacunae 900-3000 μm^3.

2.5.6 Osteocyte lacunar morphological analysis

To perform the lacunar morphological analysis, the resulting shape of a lacuna and model representation consists of a 3x3 matrix of the positions of the voxels in a lacuna. For a diagonal symmetric matrix defining an ellipsoid, this is converted into the eigenvectors of the matrix, which correspond to the major and minor axes of the ellipsoid. From the eigenvectors, the corresponding eigenvalues (EV) were derived (EV1 > EV2 > EV3), where EV1 is the largest eigenvalue and EV3 the smallest [32,33]. Three parameters were assessed to examine lacunae morphology, based on the eigenvalues of each individual lacuna: the lacuna elongation, flatness and anisotropy [34]. This nomenclature and units are summarized in Table 6. In short, lacuna elongation (EV2/EV1, ratio of medium to largest eigenvalue) ranged from lower values for elongated and 1 for spherical; lacuna flatness (EV3/EV2, ratio of smallest to medium eigenvalue) ranged from 0 for flat to 1 for spherical; and lacuna anisotropy (1-EV3/EV1, one minus the ratio of smallest to largest eigenvalue) ranged from 0 for isotropic/spherical to 1 for highest anisotropy.

2.6 Statistical analysis

A total of n=15 bone biopsy samples were analyzed, including MGUS n=3, SMM n=2, newly diagnosed MM n=6 and control biopsy samples n=4 (Jamshidi n=1 and from autopsies n=3). Additional bone biopsy samples (n>15) were collected but excluded from the analysis due to lack of sample integrity (e.g. loss of bone structure (bone debris) during the extraction procedure) or insufficient amount of trabecular bone. To analyze the differences in bone microporosity and lacunar morphological analysis, a one-way analysis of variance (ANOVA) with Tukey's multiple comparisons test (*$p<0.05$) was used (GraphPad Prism 8.0 software).

3. Results

3.1 Clinical data and patient history

Clinical data from patients from the University Hospital Würzburg and parameters describing bone metabolism are compiled in Tables 1-3. The cohort included patient-derived bone biopsy samples with the precursor condition MGUS (Table 1), SMM (Table 2), and newly diagnosed MM (Table 3). MGUS is diagnosed when monoclonal immunoglobulins (< 3

294 g/dL) are detected in the serum of patients and less than 10% abnormal plasma cells are
295 found in the bone marrow. When MGUS continuously progresses, the condition is named
296 SMM, when between 10-60% plasma cells are detected and monoclonal immunoglobulin
297 levels are higher than 3 g/dL. SMM differs from symptomatic MM, a stage in which
298 C.R.A.B. symptoms of hypercalcemia, renal insufficiency, anemia and osteolytic bone
299 lesions occur [35]. The revised International Staging System for Multiple myeloma (r-ISS) was
300 used to stratify patients with respect to their survival (Tables 1-3) [36]. Control samples
301 obtained from the University Hospital Würzburg and from the Ludwig Boltzmann-Institute of
302 Osteology Vienna are compiled in Table 4.
303
304 Patients with MGUS showed no detectable osteolytic bone lesions by low-dose CT scans
305 (Table 1). One patient with MGUS received denosumab for four months (MGUS1, Table 1).
306 In this case, we cannot exclude that the anti-resorptive treatment interfered with the bone
307 ultrastructure. Similarly, the two patients classified as SMM exhibited no signs of osteolytic
308 lesions by low-dose CT scans at the time of biopsy (Table 2). Disease staging for SMM was
309 determined based on the percent of bone marrow infiltration of $CD138^+$ plasma cells, above
310 10%. Patients classified as MM had a bone marrow infiltration of $CD138^+$ plasma cells
311 between 60-90% (4 out of 6), a ratio of the involved to the uninvolved free light chain in the
312 serum (sFLC) of >100 (2 out of 6), and/or local or disseminated lytic lesions, as well as
313 reduced bone mineral density (4 out of 6 patients) based on CT findings (Table 3). All bone
314 turnover markers (phosphate, calcium, alkaline phosphatase) were within normal ranges
315 (Tables 1-3). Anti-resorptive therapy with the bisphosphonate zoledronic acid had been
316 administered to one MM patient for one month before the biopsy was taken (MM1, Table 3).
317 We assume that the single dose of the bisphosphonate did not affect bone ultrastructure in
318 such short timeframe.
319
320 **3.2 Immunohistochemical (IHC) and microcomputed tomography (microCT) overview**
321 **analysis**
322 As part of the standard clinical practice, and to detect the clonal bone marrow plasma cells
323 and quantify the percent of bone marrow infiltration of $CD138^+$ cells, bone biopsies were
324 processed for immunohistochemical (IHC) analysis for CD138 staining. Fig. 1a-c shows
325 representative samples of MGUS, SMM and newly diagnosed MM patients with <10% for
326 MGUS and >10% for SMM and MM patients. Biopsies collected from patients were selected
327 after applying exclusion criteria (see section 4.6 for details). 3D reconstructions of

representative images are shown in Fig. 1d-f. Quantification of trabecular thickness distribution is shown in Fig. 1g-j and Supplementary Figure S1. No clear differences between MGUS, SMM and newly diagnosed MM were observed in the macroscopic trabecular bone architecture, which motivated the further analysis of bone ultrastructure with high resolution microCT.

3.3 Bone ultrastructure and segmentation of osteocyte lacunar microporosity

We next investigated the bone ultrastructure with a focus on the osteocyte lacunar microporosity. High resolution microCT scans (voxel size 1-2 µm) were performed on smaller volumes of interest (VOI) (Supplementary Figure S2). Figure 2 illustrates an example of VOI of representative samples and the segmented osteocyte lacunar microporosity for MGUS, SMM and newly diagnosed MM, and Supplementary Figure S3 for a control sample. This segmented osteocyte lacunar microporosity was then quantitatively analyzed for lacunar volume distribution (Fig. 3-4), lacunar density and microporosity (Fig. 5), and lacunar morphological analysis (Fig. 6).

3.4. Analysis of osteocyte lacunar volume distribution and microporosity

First, we characterized the osteocyte lacunar volume distribution, first as a frequency distribution (Fig. 3) and then as a cumulative distribution (Fig. 4). To plot the lacunar volume frequency distribution, all lacunae within one sample were stratified according to volume intervals of 20 μm^3. Two separate lacunar volume ranges were investigated: small lacunae 20-900 μm^3 (Fig. 3a-c) (osteocyte lacunar microporosity characteristic of healthy bone [28,31]), and larger lacunae 900-3000 μm^3 (Fig. 3d-f) (microporosity potentially associated to bone disease). Control samples (Fig. 3a, d) were compared with MGUS, SMM (Fig. 3b, e), and newly diagnosed MM (Fig. 3c, f). In the small lacunae range 20-900 μm^3, we observed a distribution within a comparable range (y-axis from 0-4000 μm^3) in the different groups, with the exception of sample #MM 3, which had a much higher number of osteocyte lacunae compared to the other samples within the MM group (Fig. 3c, note the extended y-axis). In contrast, in the larger lacunae range 900-3000 μm^3, we observe a clearly higher number of lacunae for the MM group (Fig. 3f) compared with MGUS (Fig. 3d) and SMM (Fig. 3e) groups.

When comparing both ranges, we observed a larger number of small osteocyte lacunae (Fig. 3a-c) compared to larger lacunae (Fig. 3d-f). This motivated a more detailed lacunar volume cumulative distribution analysis (Fig. 4), where the lacunar number (Lc.N) was plotted as a cumulative curve. The 50% cutoff indicates that half of all osteocyte lacunae within one sample are below that specific volume interval (x-axis). In the control group (Fig. 4a), the 50% cutoff is heterogeneous: samples #control 1, #control 3 and #control 4 have 50% of the lacunae with volumes around 140-170 μm^3, while sample #control 2 has the highest volume with 270 μm^3. In the MGUS/SMM group (Fig. 4b), the 50% cutoff ranges from 170-210 μm^3, except sample #SMM 2 with the smallest cutoff at 140 μm^3. In the MM group (Fig. 4c), the 50% cutoff varies from 150-220 μm^3, with clearly lower values for the biopsies of patients without bone osteolytic lesions (#MM 3 and #MM 6). In conclusion, we observe a trend for increasing 50% cutoff for more advanced disease, indicating that the sum volume of the smallest 50% lacunae account for a larger volume as the disease progresses (Fig. 4c). In other words, we observe a shift towards larger lacunae with disease progression.

Next, we calculated the lacunar density as the total number of osteocyte lacunae (Lc.TN) normalized to the trabecular bone total volume and excluding lacunar total volume (Tb.TV-Lc.TV), in other words, the sum of the osteocyte lacunar volume frequency distribution (Fig. 3). This was done for both ranges separately, small lacunae 20-900 μm^3 (Fig. 5a) and larger lacunae 900-3000 μm^3 (Fig. 5b). In the small lacunae range, the mean for the control samples was 29809 +/- 11314 lacunae/mm^3, for MGUS/SMM 18165 +/- 3278 lacunae/mm^3 and for MM 20502 +/- 13827 lacunae/mm^3. No significant differences were observed in the small lacunae range, although there was a clear trend for lower lacunar density for diseased samples (MGUS/SMM and MM) compared to the controls. However, in the larger lacunae range 900-3000 μm^3 (Fig. 5b), significantly higher lacunar density was found in the newly diagnosed MM group compared to the MGUS/SMM group.

In order to evaluate the microporosity in relation to the total bone volume, we divided the lacunar total volume (Lc.TV) by trabecular bone total volume (Tb.TV) for each group. This was done for both ranges separately, small lacunae 20-900 μm^3 (Fig. 5c) and larger lacunae 900-3000 μm^3 (Fig. 5d). No significant differences were observed in the small lacunae range. However, in the larger lacunae range, significantly higher microporosity was found in the

392 newly diagnosed MM group compared to the MGUS/SMM group. This is consistent with the
393 observations of lacunar volume frequency distribution (Fig. 3f) and lacunar density (Fig. 5b).
394
395 **3.5 Analysis of osteocyte lacunar morphology**
396 Next, we aimed to assess whether disease progression could be associated with lacunar
397 morphological changes. To do so, we performed a lacunar morphological analysis in the
398 small lacunae 20-900 μm^3 range in all groups (control, MGUS/SMM and newly diagnosed
399 MM). Based on previous analogous analysis [34], we investigated the distribution of lacunar
400 flatness, elongation and anisotropy. Towards that end, the principal eigenvalues for each
401 osteocyte lacunae were obtained: EV1, EV2 and EV3. The morphological parameters were
402 calculated as described in Table 6. The lacuna elongation (EV2/EV1, ratio of medium to
403 largest eigenvalue) is shown in Fig. 6a-d; lacuna flatness (EV3/EV2, ratio of smallest to
404 medium eigenvalue) in Fig. 6e-h; and lacuna anisotropy (1-EV3/EV1, one minus the ratio of
405 smallest to largest eigenvalue) in Fig. 6i-l. The fraction of lacunar number (Lc.N) normalized
406 against lacunae total number (Lc.TN) in each sample is shown for each group: control (Fig.
407 6a, e, i), MGUS/SMM (Fig. 6b, f, j) and MM (Fig. 6c, g, k). The median of all lacuna
408 elongation values for each sample are shown in Fig. 6d; similarly, for flatness in Fig. 6h and
409 anisotropy in Fig. 6l.
410
411 Lacuna flatness in MGUS/SMM and newly diagnosed MM groups exhibit a broader spread
412 of the distribution compared to the control group, with a shift towards lower values (flatter
413 shapes). Regarding lacuna elongation and anisotropy, the spread of the distribution for the
414 three groups is comparable. A trend for lower values for lacuna elongation (more elongated)
415 and higher values for lacuna anisotropy (more anisotropic) is observed in the MGUS/SMM
416 group compared to the control group, as shown by the curves and the by the median values.
417 However, the differences of the median values are not significant.
418
419 **4. Discussion**
420 Changes in the volume and shape of osteocytes were identified in previous studies of bone
421 metastasis from breast and prostate cancer and were indicators of osteolysis [13–16]. However,
422 high resolution microCT characterization of osteocyte lacunae in human bone biopsies of
423 MGUS, SMM and newly diagnosed MM has not yet been performed, nor have changes in
424 morphology of osteocytes been linked to patterns of osteolysis and disease progression. In
425 this context, quantitative analyses of microCT demonstrate altered lacunae volume and shape

426 distribution between MGUS, SMM and newly diagnosed MM. Specifically, we found a
427 significantly higher number of larger lacunae in the 900-3000 μm^3 range, in the MM group
428 compared to the MGUS/SMM group, as reflected in higher lacunar volume frequency
429 distribution (Fig. 3f) and significantly higher lacunar density (Fig. 5b). Consistent with the
430 observation of an increase in lacunar volume frequency distribution, we also found
431 significantly higher microporosity for the larger lacunae range in the MM group compared to
432 the MGUS/SMM group (Fig. 5d).
433
434 In the small lacunae 20-900 μm^3 range, the lacunar density for control samples with 29809
435 +/- 11314 lacunae/mm^3 (Fig. 5a) is in the range previously reported in the literature for 3D
436 analysis of osteocyte morphometry in healthy transiliac bone biopsies [28], which confirms the
437 validity of our analysis. Interestingly, there was a trend for lower lacunar density for diseased
438 samples (MGUS/SMM and MM) compared to the controls, though the differences were not
439 significant (Fig. 5a). This could be indicative of micropetrosis, i.e. osteocyte lacunae
440 mineralization following osteocyte apoptosis [37,38]. Since a lower lacunar density can
441 distinguish healthy, osteoporotic and bisphosphonate-treated osteoporotic patients, it is
442 currently being considered as a novel bone microstructural marker of impaired bone quality
443 [37]. In addition, we observed a trend for increasing values of the 50% cutoff in the lacunar
444 volume cumulative distribution for more advanced disease, showing that the sum volume of
445 the smallest 50% lacunae account for a larger volume as the disease progresses (Fig. 4). In
446 terms of shape distribution, the MGUS/SMM group showed a trend for lower lacuna flatness
447 (flatter), lower lacuna elongation (more elongated), and higher lacuna anisotropy (more
448 anisotropic) compared to the control group (Fig. 6). Altogether, the findings of a trend for
449 lower lacunar density and a shift towards larger lacunae (increasing 50% cutoff of the lacunar
450 volume cumulative distribution) for diseased samples diseased samples (MGUS/SMM and
451 MM) compared to control, in the small lacunae 20-900 μm^3 range; together with significantly
452 higher lacunar density and microporosity for the newly diagnosed MM group, in the larger
453 lacunae 900-3000 μm^3 range, suggest that the osteocytes in MM bone disease and the
454 precursor conditions MGUS/SMM are undergoing changes in their lacunae morphology
455 during disease progression.
456
457 In relation to previous work, currently this is the first study evaluating human bone biopsies
458 at the microstructural level, and so we can only refer to similar work in preclinical setting.

459 Indeed, our established mouse model of MM bone disease was assessed for ultrastructural
460 characterization of the mineralized and nonmineralized ECM, particularly of the osteocyte
461 LCN in early stages of the disease [27,39–41]. Skeletally mature mice were injected with MM
462 cells and the osteocyte LCN architecture was analyzed using advanced imaging techniques,
463 such as high resolution microCT, synchrotron phase contrast-enhanced microCT and
464 confocal laser scanning microscopy (CLSM) [27]. Similar as in human samples, we identified
465 alterations in the osteocyte morphology in the early MM lesions and showed larger, irregular-
466 shaped osteocyte lacunae within a disorganized canaliculi network, compared to flat
467 osteocyte lacunae organized in a lamellar structure in healthy bone [27]. MM affected regions
468 revealed that the lacunae volume was greater and the density was sparser compared to control
469 bones [27]. These data are in concordance with the human MM samples in which a higher
470 number of larger lacunae and a lower lacunar density were detected in the MM group
471 compared to the precursor conditions and control samples. Overall, the MM preclinical model
472 served to predict the changes in the osteocyte lacunae, which in human bone biopsies
473 occurred as a result of progression from MGUS to MM, and thus aligning the preclinical
474 observations with the human findings.
475
476 In a recent study in immunocompetent mice, breast and prostate cancer cells were
477 intratibially injected and the changes in the osteocyte LCN induced by tumor cells were
478 analyzed by histology, microCT imaging and CLSM [20]. Interestingly, large lacunae and
479 vascular canals were not observed in the proximity of osteolytic lesions, whereas these
480 changes occurred in osteosclerotic lesions adjacent to prostate cancer cells [20], indicating that
481 changes of osteocyte lacunae characteristics are tumor type-specific. In our study of human
482 biopsy samples with newly diagnosed MM and the precursor conditions, we observed a
483 significantly higher lacunar density in the MM group compared to the MGUS/SMM groups.
484 These observed changes may be related to the presence of osteocytic osteolysis [42], a process
485 that involves osteocytes mobilizing calcium and phosphate, using carbonic anhydrase and
486 vacuolar ATPase to demineralize the bone matrix, and digest protein using matrix
487 metalloproteases and tartrate-resistant acid phosphatase (TRAP) [20,43–45]. In the above-
488 mentioned mouse model [20], TRAP-positive osteocytes in combination with large lacunae
489 were detected in osteosclerotic regions of breast and prostate infiltrated bones, indicating that
490 this mechanism could contribute to the observed increase in lacunae volume [20,43–45]. Whether
491 osteocytic osteolysis plays a role in the progression from healthy to MGUS/SMM to MM
492 bone is not known and warrants further studies. Moreover, since the osteocyte remodeling

493 function affects the lacunae morphology and the LCN architecture, it is likely that changes in
494 the latter are indicators for impaired bone remodeling activity and mechanoresponsiveness.
495
496 In order to understand the implications of altered lacunae volume and shape distribution in
497 MM, future studies should consider several factors. First, there is a need for more bone
498 biopsies in i) each of the groups and ii) with sufficient quality to obtain a larger sample size
499 and validate the findings of this study, iii) at other sites of the skeleton where imaging, for
500 example via PET-CT, has shown infiltration of the bone, and iv) from males and females at
501 the ratio of the occurrence of the disease. Second, it is important that the bone biopsies are
502 obtained from comparable anatomical sites to minimize the natural osteocyte volume and
503 shape variation within healthy bone [8,28,46]. Third, although previous studies have used a
504 comparable voxel size of 1.2 µm for lacunar imaging in human bone biopsies [11,28], to further
505 investigate the relationship between osteocyte lacunae and MM, researchers could increase
506 the volume of interest scanned at high resolution (1 µm voxel size or lower) using
507 synchrotron phase-contrast microCT. Fourth, there is a lack of detailed information whether
508 the biopsies were extracted from bone regions affected or unaffected by the disease.
509 Therefore, it remains uncertain whether the evaluated osteocytes accurately reflect the disease
510 stage. For ethical and practical considerations, the bone samples used in the present study
511 were extracted through a standardized approach from the posterior superior iliac crest.
512 Finally, the use of mouse models of MM may provide a valuable tool for investigating the
513 mechanisms underlying the observed alterations in osteocyte lacunae morphology and other
514 aspects of bone ultrastructure, such as LCN architecture, bone composition, and micro- and
515 nanoscale organization of the organic and inorganic matrix. Furthermore, these models can be
516 used to study how alterations of the osteocyte lacunar morphology affect the response of
517 osteocytes to local tissue strains, their remodeling capacity of mineralized bone matrix and
518 the associated resistance to fractures.
519
520 Taken together, these findings suggest that altered lacunae volume and shape distribution are
521 indicative for osteolysis and disease progression from MGUS, SMM to newly diagnosed
522 MM. Future studies are needed to explore whether such changes cause lower local tissue
523 strains and an impaired bone mechanoresponse in MM patients with osteolytic bone lesions
524 and an associated high fracture risk.
525

5. Conflict of interest

The authors declare no conflict of interest.

6. Data availability

The raw/processed data required to reproduce these findings are available in the publicly accessible Edmond repository of the Max Planck Society (https://doi.org/10.17617/3.5BPJUP).

7. Author contributions

A Cipitria, I. Moreno-Jiménez and F. Jundt conceived the idea. I. Moreno-Jiménez and S. Heinig processed the bone biopsy samples and performed the experiments. D. Maichl collected and prepared the human Jamshidi bone biopsy samples. S. Strifler educated patients about and performed the biopsies, and collected clinical data. E. Leich curated clinical data related to the human bone biopsy samples; S. Blouin provided the control bone autopsy samples. I. Moreno-Jiménez, S. Heinig, U. Heras, F. Jundt and A. Cipitria analyzed the data. P. Fratzl and N. Fratzl-Zelman together with A Cipitria, I. Moreno-Jiménez and F. Jundt evaluated the methods and results. A Cipitria, I. Moreno-Jiménez and F. Jundt drafted the manuscript. All authors discussed the results and contributed to the final manuscript.

8. Funding

This research was funded by a postdoctoral research fellowship from the Humboldt Foundation (I.M.-J.) and by the Deutsche Forschungsgemeinschaft (DFG) Emmy Noether grant CI 203/2-1 (A.C). A.C. also thanks the funding from IKERBASQUE Basque Foundation for Science; from the Spanish Ministry of Science and Innovation, grant PID2021-123013OB-I00 funded by MCIN/AEI/10.13039/501100011033/FEDER, UE; from the Fundación Científica Asociación Española Contra el Cáncer (grant number LABAE223466CIPI) and from Osasun Saila, Eusko Jaurlaritza (grant 2023333027). This work was supported by the Interdisciplinary Center for Clinical Research (IZKF), Medical Faculty of Würzburg, grant B-409 (F.J.) and the German Research Foundation (DFG) grants JU426/10-1 (F.J., 491715122) and JU 426/11-1 (F.J., 496963451). E.L. was supported by a grant of the Deutsche Krebshilfe (70112693).

9. Acknowledgements

The authors thank Daniel Werner, Jeannette Steffen, Daniela S. Garske and Susann Weichold at the Max Planck Institute of Colloids and Interfaces in Potsdam for their technical assistance.

References

1. Bonewald, L. F. The amazing osteocyte. *Journal of Bone and Mineral Research* **26,** 229–238 (2011).
2. Hemmatian, H., Bakker, A. D., Klein-Nulend, J. & van Lenthe, G. H. Aging, osteocytes, and mechanotransduction. *Curr Osteoporos Rep* **15,** 401–411 (2017).
3. Gerbaix, M., Gnyubkin, V., Farlay, D., Olivier, C., Ammann, P., Courbon, G., Laroche, N., Genthial, R., Follet, H., Peyrin, F., Shenkman, B., Gauquelin-Koch, G. & Vico, L. One-month spaceflight compromises the bone microstructure, tissue-level mechanical properties, osteocyte survival and lacunae volume in mature mice skeletons. *Sci Rep* **7,** 2659 (2017).
4. Lane, N. E., Yao, W., Balooch, M., Nalla, R. K., Balooch, G., Habelitz, S., Kinney, J. H. & Bonewald, L. F. Glucocorticoid-treated mice have localized changes in trabecular bone material properties and osteocyte lacunar size that are not observed in placebo-treated or estrogen-deficient mice. *Journal of Bone and Mineral Research* **21,** 466–476 (2005).
5. Tiede-Lewis, L. M. & Dallas, S. L. Changes in the osteocyte lacunocanalicular network with aging. *Bone* **122,** 101–113 (2019).
6. Tommasini, S. M., Trinward, A., Acerbo, A. S., De Carlo, F., Miller, L. M. & Judex, S. Changes in intracortical microporosities induced by pharmaceutical treatment of osteoporosis as detected by high resolution micro-CT. *Bone* **50,** 596–604 (2012).
7. Mullender, M. G., van der Meer, D. D., Huiskes, R. & Lips, P. Osteocyte density changes in aging and osteoporosis. *Bone* **18,** 109–113 (1996).
8. Blouin, S., Misof, B. M., Mähr, M., Fratzl-Zelman, N., Roschger, P., Lueger, S., Messmer, P., Keplinger, P., Rauch, F., Glorieux, F. H., Berzlanovich, A., Gruber, G. M., Brugger, P. C., Shane, E., Recker, R. R., Zwerina, J. & Hartmann, M. A. Osteocyte lacunae in transiliac bone biopsy samples across life span. *Acta Biomater* **157,** 275–287 (2023).
9. Milovanovic, P., Zimmermann, E. A., Riedel, C., Scheidt, A. vom, Herzog, L., Krause, M., Djonic, D., Djuric, M., Püschel, K., Amling, M., Ritchie, R. O. & Busse, B. Multi-level characterization of human femoral cortices and their underlying osteocyte network reveal trends in quality of young, aged, osteoporotic and antiresorptive-treated bone. *Biomaterials* **45,** 46–55 (2015).
10. Hemmatian, H., Bakker, A. D., Klein-Nulend, J. & van Lenthe, G. H. Alterations in osteocyte lacunar morphology affect local bone tissue strains. *J Mech Behav Biomed Mater* **123,** 104730 (2021).
11. Yang, K. G., Goff, E., Cheng, K. lo, Kuhn, G. A., Wang, Y., Cheng, J. C. yiu, Qiu, Y., Müller, R. & Lee, W. Y. wai. Abnormal morphological features of osteocyte lacunae in adolescent idiopathic scoliosis: A large-scale assessment by ultra-high-resolution micro-computed tomography. *Bone* **166,** 116594 (2023).
12. Atkinson, E. G. & Delgado-Calle, J. The emerging role of osteocytes in cancer in bone. *JBMR Plus* **3,** e10186 (2019).
13. Adhikari, M. & Delgado-Calle, J. Role of osteocytes in cancer progression in the bone and the associated skeletal disease. *Curr Osteoporos Rep* **19,** 247–255 (2021).

14. Hofbauer, L. C., Bozec, A., Rauner, M., Jakob, F., Perner, S. & Pantel, K. Novel approaches to target the microenvironment of bone metastasis. *Nat Rev Clin Oncol* **18,** 488–505 (2021).
15. Mastro, A. M., Gay, C. V., Welch, D. R., Donahue, H. J., Jewell, J., Mercer, R., DiGirolamo, D., Chislock, E. M. & Guttridge, K. Breast cancer cells induce osteoblast apoptosis: A possible contributor to bone degradation. *J Cell Biochem* **91,** 265–276 (2004).
16. Hemmatian, H., Conrad, S., Furesi, G., Mletzko, K., Krug, J., Faila, A. V., Kuhlmann, J. D., Rauner, M., Busse, B. & Jähn-Rickert, K. Reorganization of the osteocyte lacuno-canalicular network characteristics in tumor sites of an immunocompetent murine model of osteotropic cancers. *Bone* **152,** 116074 (2021).
17. Roodman, G. Pathogenesis of myeloma bone disease. *Blood Cells Mol Dis* **32,** 290–292 (2004).
18. Berenson, J., Rajdev, L. & Broder, M. Bone complications in multiple myeloma. *Cancer Biol Ther* **5,** 1082–1085 (2006).
19. Terpos, E., Ntanasis-Stathopoulos, I. & Dimopoulos, M. A. Myeloma bone disease: from biology findings to treatment approaches. *Blood* **133,** 1534–1539 (2019).
20. Delgado-Calle, J., Anderson, J., Cregor, M. D., Hiasa, M., Chirgwin, J. M., Carlesso, N., Yoneda, T., Mohammad, K. S., Plotkin, L. I., Roodman, G. D. & Bellido, T. Bidirectional notch signaling and osteocyte-derived factors in the bone marrow microenvironment promote tumor cell proliferation and bone destruction in multiple myeloma. *Cancer Res* **76,** 1089–1100 (2016).
21. Huston, A. & Roodman, G. D. Role of the microenvironment in multiple myeloma bone disease. *Future Oncology* **2,** 371–378 (2006).
22. Rajkumar, S. V., Dimopoulos, M. A., Palumbo, A., Blade, J., Merlini, G., Mateos, M.-V., Kumar, S., Hillengass, J., Kastritis, E., Richardson, P., Landgren, O., Paiva, B., Dispenzieri, A., Weiss, B., LeLeu, X., Zweegman, S., Lonial, S., Rosinol, L., Zamagni, E., Jagannath, S., Sezer, O., Kristinsson, S. Y., Caers, J., Usmani, S. Z., Lahuerta, J. J., Johnsen, H. E., Beksac, M., Cavo, M., Goldschmidt, H., Terpos, E., Kyle, R. A., Anderson, K. C., Durie, B. G. M. & Miguel, J. F. S. International myeloma working group updated criteria for the diagnosis of multiple myeloma. *Lancet Oncol* **15,** e538–e548 (2014).
23. Borggrefe, J., Giravent, S., Campbell, G., Thomsen, F., Chang, D., Franke, M., Günther, A., Heller, M. & Wulff, A. Association of osteolytic lesions, bone mineral loss and trabecular sclerosis with prevalent vertebral fractures in patients with multiple myeloma. *Eur J Radiol* **84,** 2269–2274 (2015).
24. Lee, E. M. & Kim, B. Clinical significance of trabecular bone score for prediction of pathologic fracture risk in patients with multiple myeloma. *Osteoporos Sarcopenia* **4,** 73–76 (2018).
25. Takasu, M., Tani, C., Ishikawa, M., Date, S., Horiguchi, J., Kiguchi, M., Tamura, A., Sakai, A., Asaoku, H., Nango, N. & Awai, K. Multiple Myeloma: Microstructural Analysis of Lumbar Trabecular Bones in Patients without Visible Bone Lesions—Preliminary Results. *Radiology* **260,** 472–479 (2011).
26. Michels, M., Morais-Faria, K., Rivera, C., Brandão, T. B., Santos-Silva, A. R. & Oliveira, M. L. Structural complexity of the craniofacial trabecular bone in multiple myeloma assessed by fractal analysis. *Imaging Sci Dent* **52,** 33–41 (2022).
27. Ziouti, F., Soares, A. P., Moreno-Jiménez, I., Rack, A., Bogen, B., Cipitria, A., Zaslansky, P. & Jundt, F. An early myeloma bone disease model in skeletally mature mice as a platform for biomaterial characterization of the extracellular matrix. *J Oncol* **2020,** 1–12 (2020).

28. Goff, E., Cohen, A., Shane, E., Recker, R. R., Kuhn, G. & Müller, R. Large-scale osteocyte lacunar morphological analysis of transiliac bone in normal and osteoporotic premenopausal women. *Bone* **160,** 116424 (2022).
29. Carter, Y., Thomas, C. D. L., Clement, J. G. & Cooper, D. M. L. Femoral osteocyte lacunar density, volume and morphology in women across the lifespan. *J Struct Biol* **183,** 519–526 (2013).
30. Buenzli, P. R. & Sims, N. A. Quantifying the osteocyte network in the human skeleton. *Bone* **75,** 144–150 (2015).
31. McCreadie, B. R., Hollister, S. J., Schaffler, M. B. & Goldstein, S. A. Osteocyte lacuna size and shape in women with and without osteoporotic fracture. *J Biomech* **37,** 563–572 (2004).
32. Gescheidtova, E., Marcon, P., Bartusek, K., Gescheidtová, E., Marcon, P. & Bartusek, K. Visualization of plant fibres via diffusion tensor imaging. in *PIERS Proceedings, Suzhou, China* (2011). at <https://www.researchgate.net/profile/Karel-Bartusek/publication/267556847_Visualization_of_Plant_Fibres_via_Diffusion_Tensor_Imaging/links/5583ec1a08ae89172b861a80/Visualization-of-Plant-Fibres-via-Diffusion-Tensor-Imaging.pdf>
33. Mader, K. S., Schneider, P., Müller, R. & Stampanoni, M. A quantitative framework for the 3D characterization of the osteocyte lacunar system. *Bone* **57,** 142–154 (2013).
34. Chaumel, J., Schotte, M., Bizzarro, J. J., Zaslansky, P., Fratzl, P., Baum, D. & Dean, M. N. Co-aligned chondrocytes: Zonal morphological variation and structured arrangement of cell lacunae in tessellated cartilage. *Bone* **134,** 115264 (2020).
35. Bernstein, Z. S., Kim, E. B. & Raje, N. Bone Disease in Multiple Myeloma: Biologic and Clinical Implications. *Cells 2022, Vol. 11, Page 2308* **11,** 2308 (2022).
36. Palumbo, A., Avet-Loiseau, H., Oliva, S., Lokhorst, H. M., Goldschmidt, H., Rosinol, L., Richardson, P., Caltagirone, S., Lahuerta, J. J., Facon, T., Bringhen, S., Gay, F., Attal, M., Passera, R., Spencer, A., Offidani, M., Kumar, S., Musto, P., Lonial, S., Petrucci, M. T., Orlowski, R. Z., Zamagni, E., Morgan, G., Dimopoulos, M. A., Durie, B. G. M., Anderson, K. C., Sonneveld, P., San Miguel, J., Cavo, M., Rajkumar, S. V. & Moreau, P. Revised International Staging System for Multiple Myeloma: A Report From International Myeloma Working Group. *Journal of Clinical Oncology* **33,** 2863–2869 (2015).
37. Milovanovic, P. & Busse, B. Phenomenon of osteocyte lacunar mineralization: indicator of former osteocyte death and a novel marker of impaired bone quality? *Endocr Connect* **9,** R70–R80 (2020).
38. Delgado-Calle, J., Bellido, T. & Roodman, G. D. Role of osteocytes in multiple myeloma bone disease. *Curr Opin Support Palliat Care* **8,** 407–413 (2014).
39. Schwarzer, R., Nickel, N., Godau, J., Willie, B. M., Duda, G. N., Schwarzer, R., Cirovic, B., Leutz, A., Manz, R., Bogen, B., Dörken, B. & Jundt, F. Notch pathway inhibition controls myeloma bone disease in the murine MOPC315.BM model. *Blood Cancer J* **4,** e217–e217 (2014).
40. Rummler, M., Ziouti, F., Bouchard, A. L., Brandl, A., Duda, G. N., Bogen, B., Beilhack, A., Lynch, M. E., Jundt, F. & Willie, B. M. Mechanical loading prevents bone destruction and exerts anti-tumor effects in the MOPC315.BM.Luc model of myeloma bone disease. *Acta Biomater* **119,** 247–258 (2021).
41. Ziouti, F., Rummler, M., Steyn, B., Thiele, T., Seliger, A., Duda, G. N., Bogen, B., Willie, B. M. & Jundt, F. Prevention of bone destruction by mechanical loading is not enhanced by the Bruton's tyrosine kinase inhibitor CC-292 in myeloma bone disease. *Int J Mol Sci* **22,** 3840 (2021).

42. Tsourdi, E., Jähn, K., Rauner, M., Busse, B. & Bonewald, L. F. Physiological and pathological osteocytic osteolysis. *J Musculoskelet Neuronal Interact* **18,** 292–303 (2018).
43. Jähn, K., Kelkar, S., Zhao, H., Xie, Y., Tiede-Lewis, L. M., Dusevich, V., Dallas, S. L. & Bonewald, L. F. Osteocytes acidify their microenvironment in response to PTHrP in vitro and in lactating mice in vivo. *Journal of Bone and Mineral Research* **32,** 1761–1772 (2017).
44. Kogawa, M., Wijenayaka, A. R., Ormsby, R. T., Thomas, G. P., Anderson, P. H., Bonewald, L. F., Findlay, D. M. & Atkins, G. J. Sclerostin regulates release of bone mineral by osteocytes by induction of carbonic anhydrase 2. *Journal of Bone and Mineral Research* **28,** 2436–2448 (2013).
45. Tang, S. Y., Herber, R.-P., Ho, S. P. & Alliston, T. Matrix metalloproteinase-13 is required for osteocytic perilacunar remodeling and maintains bone fracture resistance. *Journal of Bone and Mineral Research* **27,** 1936–1950 (2012).
46. Schemenz, V., Gjardy, A., Chamasemani, F. F., Roschger, A., Roschger, P., Zaslansky, P., Helfen, L., Burghammer, M., Fratzl, P., Weinkamer, R., Brunner, R., Willie, B. M. & Wagermaier, W. Heterogeneity of the osteocyte lacuno-canalicular network architecture and material characteristics across different tissue types in healing bone. *J Struct Biol* **212,** 107616 (2020).

726 **Figures and captions**

727 **Figure 1**

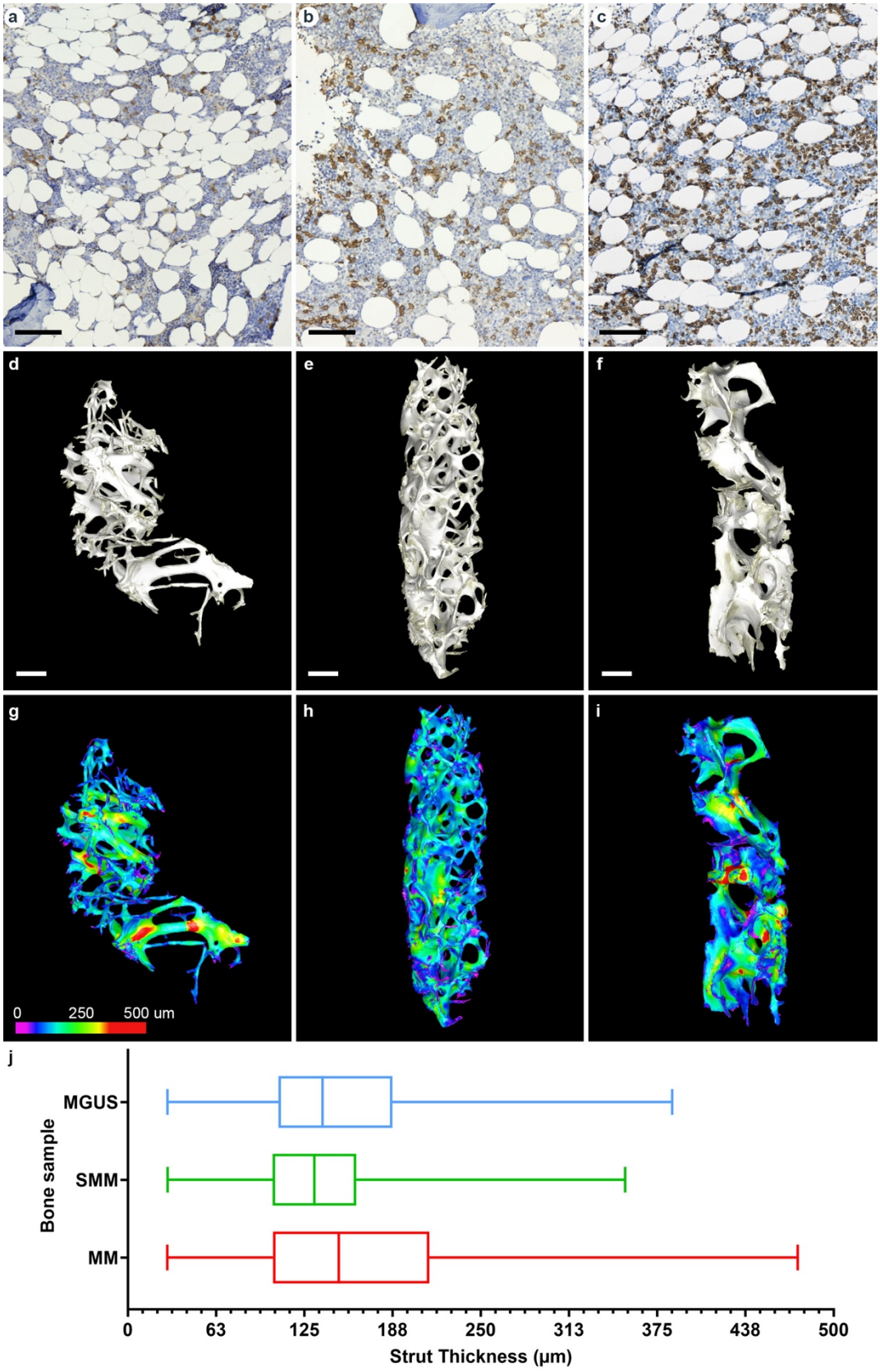

728

729 **Figure 1. Immunohistochemical (IHC) CD138 staining and low resolution microCT**
730 **overview of the bone biopsies from patients with: (a, d, g) monoclonal gammopathy of**
731 **undetermined significance (MGUS), (b, e, h) smoldering myeloma (SMM), and (c, f, i)**
732 **newly diagnosed multiple myeloma (MM).** (a-c) Representative light microscopy images of
733 the bone marrow compartment from the biopsy samples: CD138 positive staining in brown,
734 cell nuclei counterstain in blue. MGUS bone biopsy #MGUS 2 with <10% bone marrow
735 infiltration, SMM bone biopsy #SMM 1 with 10-15% bone marrow infiltration, MM bone
736 biopsy #MM 1 with 70% bone marrow infiltration. (d-f) 3D reconstructions of low resolution
737 (7 µm voxel) microCT scans of representative bone biopsies. (g-i) Quantitative analysis of
738 trabecular bone strut thickness distribution and color code visualization with Dragonfly
739 software. (j) Distribution of trabecular thickness shown with median, first and third quartile.
740 Scale bars equal to 100 µm (a-c), 1 mm (d-f).
741

742 **Figure 2**

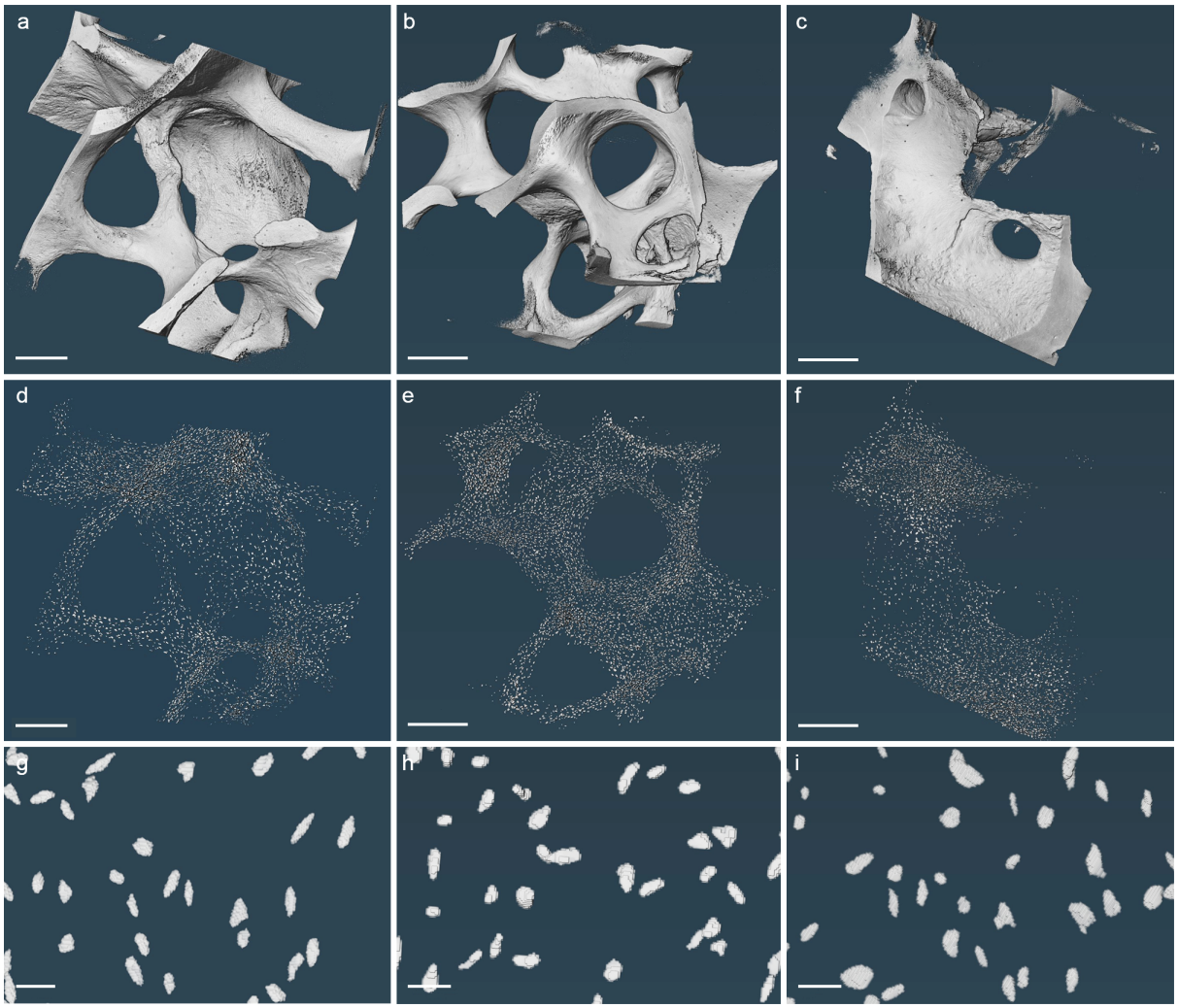

743

744 **Figure 2. Bone biopsy macroscopic structure and osteocyte lacunar microporosity**
745 **visualized with high resolution microCT in MGUS, SMM and MM samples.** (a-c) 3D
746 reconstructions of local scans (high resolution microCT; voxel size 1-2 µm) and (d-i) the
747 corresponding segmented osteocyte lacunar microporosity of representative samples: (a, d, g)
748 MGUS bone biopsy #MGUS 2, (b, e, h) SMM bone biopsy #SMM 1, (c, f, i) MM bone
749 biopsy #MM 1. Scale bars equal to 250 µm (a, d), 350 µm (b, e), 400 µm (c, f) and 20 µm (g-
750 i).
751

752 **Figure 3**

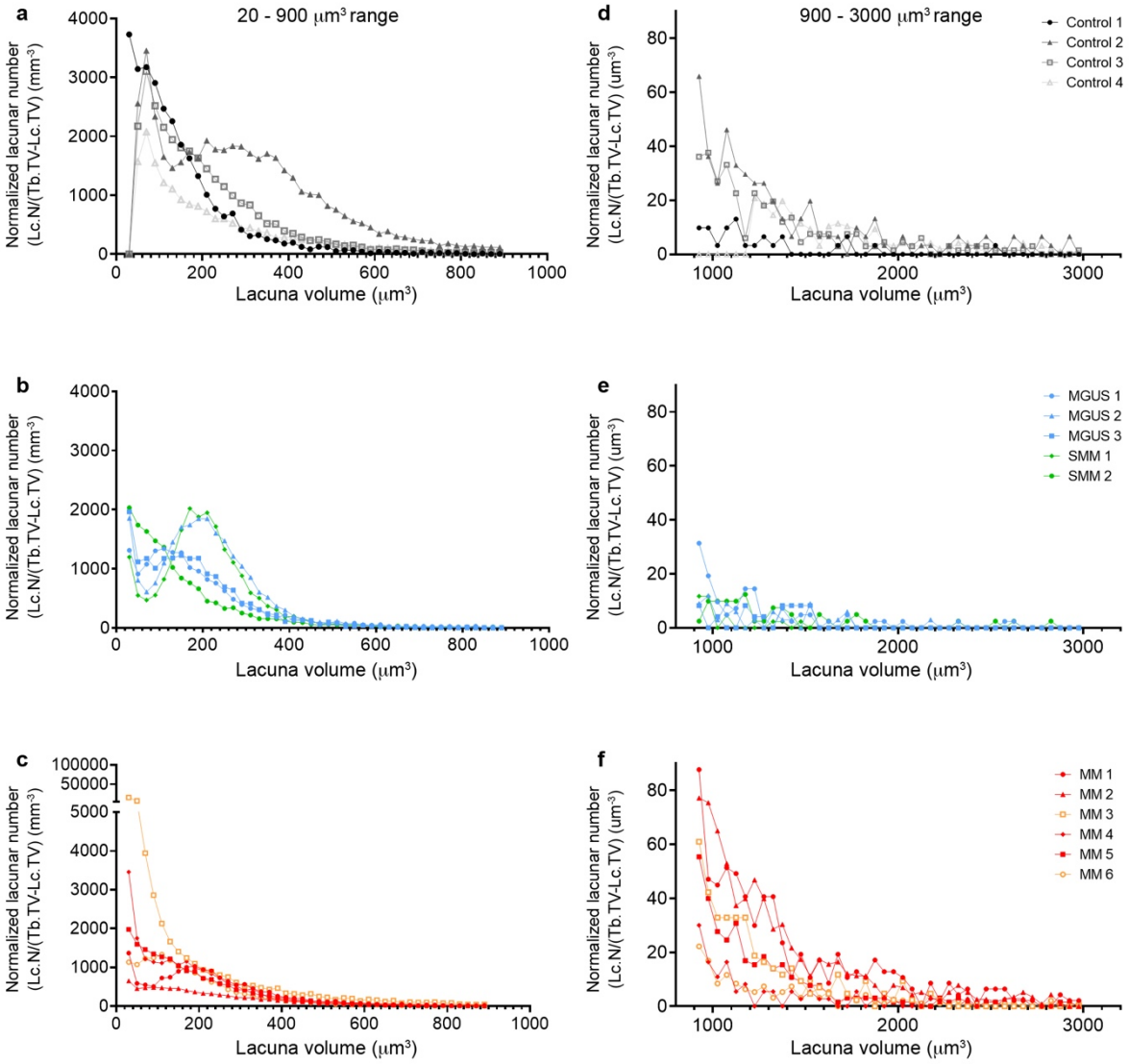

753

754 **Figure 3. Lacunar volume frequency distribution of osteocytes in control, MGUS, SMM**
755 **and MM samples.** Frequency distribution normalized to trabecular bone total volume for
756 two separate lacunar volume ranges: 20-900 μm³ and 900-3000 μm³. For each lacunae
757 volume interval (x-axis), number of osteocyte lacunae (Lc.N) normalized by the trabecular
758 bone total volume excluding lacunar total volume (Tb.TV-Lc-TV) (y-axis). Frequency
759 distribution for each group: (a, d) control, (b, e) MGUS and SMM, (c, f) MM. Sample from
760 the Jamshidi biopsy in black, all other control samples in grey. MGUS in blue, SMM in
761 green, MM samples with bone lytic lesion in red, MM samples without lytic lesions in
762 orange. Please note the different scale in the y-axis of subplot c.
763

764 **Figure 4**

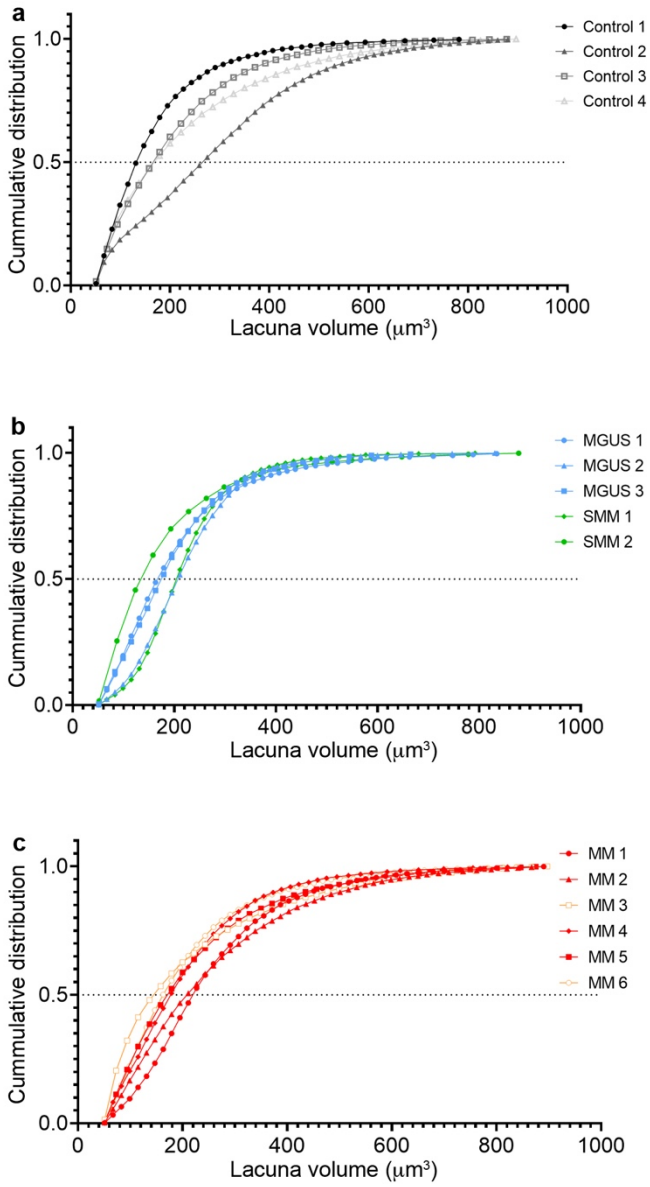

765

766 **Figure 4. Lacunar volume cumulative distribution for the small lacunae 20-900 µm³**
767 **range of osteocytes in control, MGUS, SMM and MM samples.** Cumulative distribution
768 (from 0 to 1) of lacunae (y-axis) for each volume in µm³ (x-axis). Cumulative distribution for
769 each group: (a) control, (b) MGUS and SMM, (c) MM. Dashed line indicates the 50% cutoff
770 volume below which are half of all osteocyte lacunae of one sample. Sample from the
771 Jamshidi biopsy in black, all other control samples in grey. MGUS in blue, SMM in green,
772 MM samples with bone lytic lesion in red, MM samples without lytic lesions in orange.
773

774 **Figure 5**

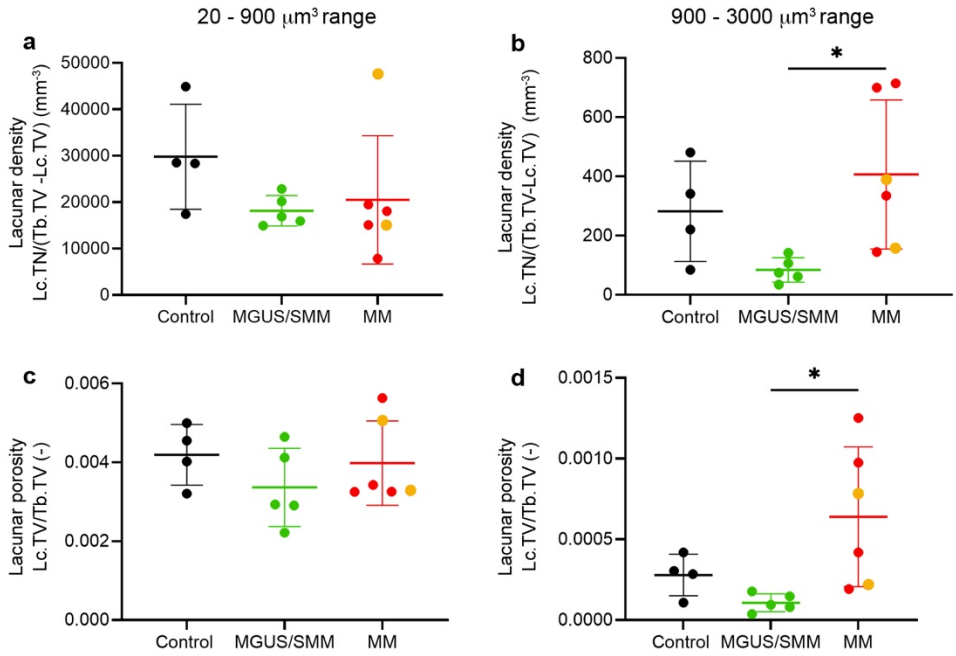

775

776 **Figure 5. Lacunar density and microporosity analysis for the small lacunae 20-900 µm³**
777 **range and for the larger lacunae 900-3000 µm³ range of osteocytes in control, MGUS,**
778 **SMM and MM samples**. Lacunar density calculated as the total number of osteocyte lacunae
779 (Lc.TN) normalized to the trabecular bone total volume and excluding lacunar total volume
780 (Tb.TV-Lc.TV), for each group control, MGUS/SMM and newly diagnosed MM (samples
781 with bone lytic lesion in red, samples without lytic lesions in orange). Microporosity
782 calculated as lacunar total volume (Lc.TV) divided by trabecular bone total volume (Tb.TV)
783 for each group. Error bars indicate mean ± SD. One way ANOVA with Tukey's multiple
784 comparison test *p<0.05.

785

786 **Figure 6**

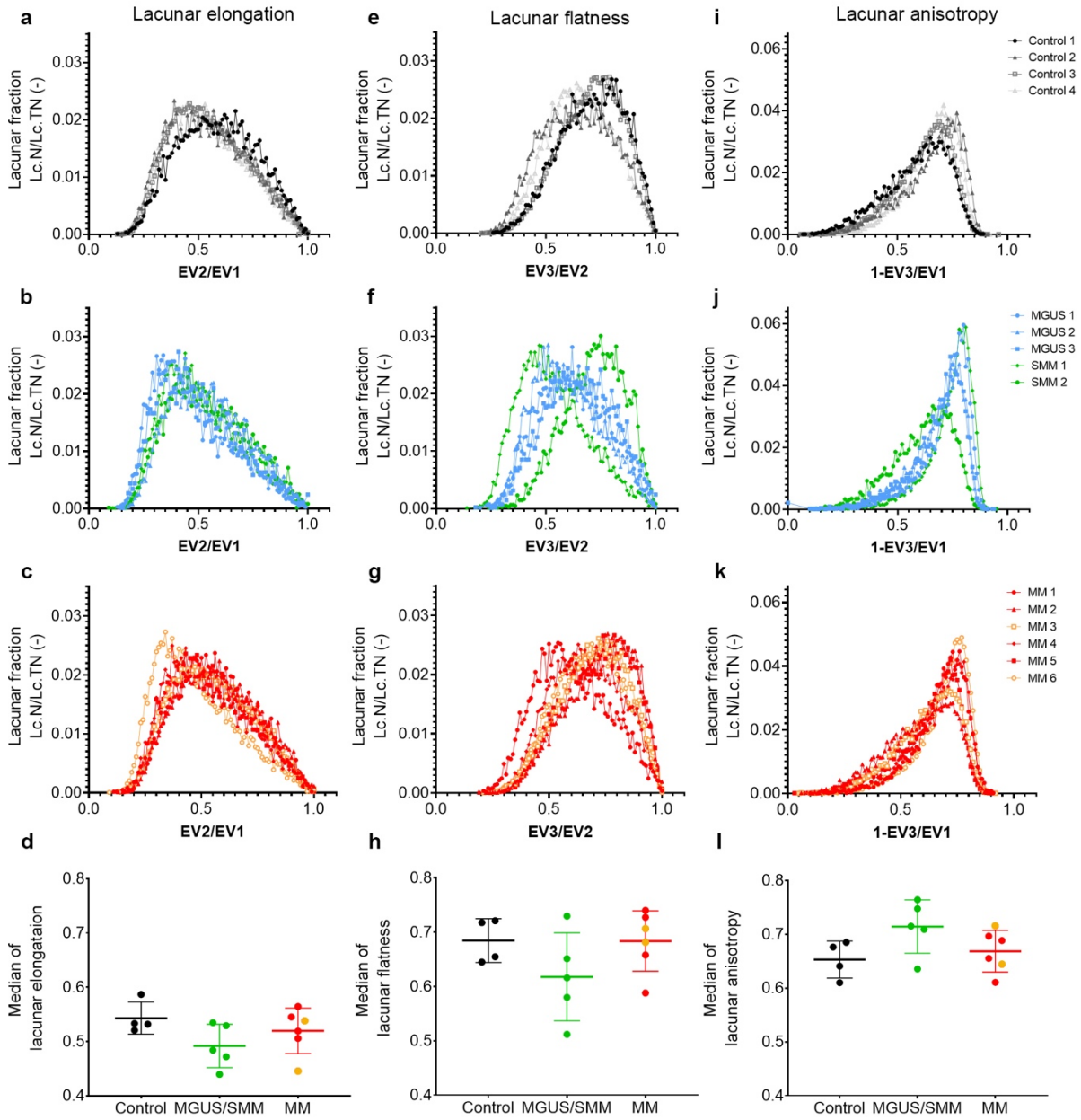

787

788 **Figure 6. Lacunar morphological analysis for the small lacunae 20-900 µm³ range of**
789 **osteocytes in control, MGUS, SMM and MM samples.** Lacunae elongation, flatness and
790 anisotropy analysis for (a, e, i) control, (b, f, j) MGUS/SMM and (c, g, k) MM groups.
791 Individual lacunae were assigned with eigenvalues (EV1, EV2 and EV3) to then calculate
792 lacuna elongation as EV2/EV1 (with lower values for elongated and 1 for spherical) as (a-c)
793 lacunar fraction (Lc.N/Lc.TN) and as (d) median of all lacuna elongation values for each
794 sample; lacuna flatness as EV3/EV2 (ranging from 0 for flat to 1 for spherical) as (e-g)
795 lacunar fraction (Lc.N/Lc.TN) and as (h) median of all lacuna flatness values for each
796 sample; and lacuna anisotropy as 1-EV3/EV1 (with smaller values for isotropic/spherical and

797 1 for highest anisotropy) as (i-k) lacunar fraction (Lc.N/Lc.TN) and as (l) median of all
798 lacuna anisotropy values for each sample. Sample from the Jamshidi biopsy in black, all other
799 control samples in grey. MGUS in blue, SMM in green, MM samples with bone lytic lesion
800 in red, MM samples without lytic lesions in orange. Error bars indicate mean ± SD.
801
802

803 **Tables**

804 **Table 1. Clinical data from MGUS patients**

Parameters			
biopsy number	MGUS 1	MGUS 2	MGUS 3
age (years)	71	60	68
gender	f	m	f
immunoglobulin subtype	IgG lambda	IgG kappa	IgG kappa
r-ISS	not applicable	not applicable	not applicable
cytogenetic risk	not applicable	not applicable	not applicable
M-protein [g/L]	not detectable	not detectable	1.2
heavy chain [mg/dL, normal range]	1382 (610-1616)*	881 (610-1616)	507 (610-1616)
involved serum free light chain (sFLC) [mg/L, normal range]	23.89 (5.71-26.30)	10.75 (3.30-19.40)	215 (3.30-19.40)
ratio (involved / uninvolved sFLC)	0.86	1.02	5.44
bone marrow infiltration of $CD138^+$ cells [%]	<10	<10	<5
CT findings of osteolytic lesion	none	none	none
hemoglobin [g/dL]	12.9 (12-16)	14.4 (13.5-16.9)	12.7 (12-16)
creatinine [mg/dL]	0.63 (0-0.95)	1.06 (0-1.17)	6.69 (0-0.95)
cytogenetics**	no aberration	no aberration	no aberration
calcium [mmol/L]	2.2 (2.0-2.7)	2.5 (2.0-2.7)	2.3 (2.0-2.7)
alkaline phosphatase [U/L]	51 (35-105)	72 (35-105)	not available
inorganic phosphate [mmol/L]	1.09 (0.87-1.45)	1 (0.87-1.45)	1.85 (0.87-1.45)
bone anti-resorption treatment (duration)	Denosumab (four months)	no	no

805 * Values in brackets show the normal range for the parameters, respectively

806 ** Cytogenetic alterations by fluorescence in situ hybridization (FISH)

807

808 **Table 2. Clinical data from SMM patients**

Parameters		
biopsy number	SMM 1	SMM 2
age (years)	46	70
gender	f	m
immunoglobulin subtype	IgA kappa	IgA lambda
r-ISS	II	I
cytogenetic risk	high risk	standard risk
M-protein [g/L]	not detectable	13.42
heavy chain [mg/dL, normal range]	1826 (88-410)	2826 (88-410)
involved serum free light chain (sFLC) [mg/L, normal range]	11.82 (3.30-19.40)	54.99 (5.71-26.3)
ratio (involved / uninvolved sFLC)	1.33	12.03
bone marrow infiltration of $CD138^+$ cells [%]	10-15	20-30
CT findings of osteolytic lesion	none	none
hemoglobin [g/dL]	12 (12-16)	13.2 (13.5-16.9)
creatinine [mg/dL]	0.78 (0-0.95)	0.91 (0-1.17)
cytogenetics	t4;14, gain of 1q21	del13q14
calcium [mmol/L]	2.2 (2.0-2.7)	2.4 (2.0-2.7)
alkaline phosphatase [U/L]	59 (35-105)	40 (35-105)
inorganic phosphate [mmol/L]	1.08 (0.87-1.45)	1.23 (0.87-1.45)
bone anti-resorption treatment (duration)	not known	no

809

810

811 **Table 3. Clinical data from newly diagnosed MM patients**

Parameters			
biopsy number	MM 1	MM 2	MM 3
age (years)	58	57	72
gender	m	m	f
immunoglobulin subtype	IgG kappa	kappa	IgG lambda
r-ISS	III	II	III
cytogenetic risk	high risk	standard risk	high risk
M-protein [g/L]	35.3	not detectable	20.6
heavy chain [mg/dL, normal range]	4765 (610-1616)	not available	3074 (610-1616)
involved serum free light chain (sFLC) [mg/L, normal range]	71.12 (3.30-19.40)	8260 (3.30-19.40)	1376 (5.71-26.3)
ratio (involved / uninvolved sFLC)	40.41	890.09	355.56
bone marrow infiltration of $CD138^+$ cells [%]	70	60-70	90
CT findings of osteolytic lesion	osteolytic lesion with extraosseous soft tissue mass in spine (T12), lytic lesion in pelvis, rib series fractures, medullary lesions in femora and humeri, reduced bone mineral density	disseminated osteolysis in spine, one large lesion in T9 with increased fracture risk, old vertebral body collapse in T7 and fracture of the fourth left rib, multiple small osteolyses in scapulae, ribs, sternum reduced bone mineral density	no osteolytic lesions medullary lesions in upper and lower limbs, spine, sternum; reduced bone mineral density
hemoglobin [g/dL]	10.8 (13.5-16.9)	10.7 (13.5-16.9)	10.2 (12-16)
creatinine [mg/dL]	0.83 (0-1.17)	2.3 (0-1.17)	0.72 (0-0.95)
cytogenetics	t14;16, gain of 1q21	t11;14	del 17p, 1q gain, del14q, del 4p, del 16q, del 5p
calcium [mmol/L]	2.3 (2.0-2.7)	2.9 (2.0-2.7)	2.5 (2.0-2.7)
alkaline phosphatase [U/L]	97 (35-105)	80 (35-105)	49 (35-105)
inorganic phosphate [mmol/L]	1.25 (0.87-1.45)	1.33 (0.87-1.45)	0.99 (0.87-1.45)
bone anti-resorption treatment (duration)	bisphosphonate (zoledronic acid)	no	no

	for one month		

Table 3 (cont). Clinical data from newly diagnosed MM patients

Parameters			
biopsy number	MM 4	MM 5	MM 6
age (years)	60	68	64
gender	m	f	f
immunoglobulin subtype	IgA lambda	IgG kappa	IgG kappa
r-ISS	II	II	II
cytogenetic risk	standard risk	standard risk	standard risk
M-protein [g/L]	32.6	4.5	7.4
heavy chain (mg/dL, normal range)	4000 (88-410)	1180 (610-1616)	1625 (610-1616)
involved serum free light chain (sFLC) [mg/L, normal range]	33.8 (5.71-26.3)	16.59 (3.30-19.40)	309.8 (3.30-19.40)
ratio (involved / uninvolved sFLC)	4.26	1.49	8.41
bone marrow infiltration of $CD138^+$ cells [%]	30	50	60
CT findings of osteolytic lesion	osteolytic lesion in pelvis; mild reduction in bone mineral density	disseminated osteolysis in skull, spine, fracture series in spine (T7, 8, 11; L1, 2, 4), reduced bone mineral density in spine	none
hemoglobin [g/dL]	14 (13.5-16.9)	10.1 (12-16)	12.8 (12-16)
creatinine [mg/dL]	0.96 (0-1.17)	1.02 (0-0.95)	0.91 (0-0.95)
cytogenetics	del 1p32, del13q14, gain of 1q21	trisomy 11	gain of 1q21
calcium [mmol/L]	2.4 (2.0-2.7)	2.5 (2.0-2.7)	2.4 (2.0-2.7)
alkaline phosphatase [U/L]	41 (35-105)	95 (35-105)	92 (35-105)
inorganic phosphate [mmol/L]	1.19 (0.87-1.45)	0.94 (0.87-1.45)	0.74 (0.87-1.45)
bone anti-resorption treatment (duration)	no	no	no

816 **Table 4. Control samples: Jamshidi bone biopsy and samples from autopsies**

Parameters				
biopsy number	control 1	control 2	control 3	control 4
type of biopsy	jamshidi	autopsy*	autopsy*	autopsy*
age (years)	69	64	57	63
gender	f	f	f	f
previous disease	myelodysplastic syndrome	not known	not known	not known

817 * Subset of an earlier cohort presented previously [8] and re-evaluated here

818
819
820 **Table 5. Nomenclature for osteocyte lacunar volume analysis**

Nomenclature	**Abbreviation**	**Unit**
Number of osteocyte lacunae	Lc.N	-
Total number osteocyte lacunae	Lc.TN	-
Lacunar volume	Lc.V	µm³
Total lacunar volume	Lc.TV	µm³
Trabecular bone total volume	Tb.TV	µm³

821
822
823 **Table 6: Nomenclature for osteocyte lacunar analysis**

Parameter	**Definition**	**Unit**	**Formula**
Normalized lacunar volume frequency distribution	Number of lacunae volume divided by the trabecular bone total volume minus the lacuna total volume	#/µm³	$\frac{\Sigma\, Lc.N}{Tb.TV\ -\ Lc.TV}$
Lacunar volume cumulative distribution	Sorted sum of volume divided by total volume	-	
Microporosity	Total lacunar volume with respect to the trabecular bone total volume	-	$\frac{Lc.TV}{Tb.TV}$
Lacuna elongation	0 for elongated 1 for spherical	-	$\frac{EV2}{EV1}$
Lacuna flatness	0 for flat 1 for spherical	-	$\frac{EV3}{EV2}$
Lacuna anisotropy	0 for isotropic, spherical 1 for highly anisotropic	-	$1 - \frac{EV3}{EV1}$

824